AN IMPROVED ZIRCALOY-STEAM REACTION MODEL FOR USE WITH THE MARCH 2 (MELTDOWN ACCIDENT RESPONSE CHARACTERISTICS) CODE

by

M. P. Manahan
Battelle, Columbus Laboratories

ABSTRACT

An improved Zircaloy-steam oxidation reaction model has been incorporated into the MARCH 2 code which includes: (1) improved physical modeling for solid-state process oxidation, (2) improved geometric modeling for gaseous diffusion oxidation, (3) chemisorption/dissociation retardation due to high hydrogen partial pressures, and (4) laminar and turbulent flow conditions. Several accident sequences have been analyzed using the model, and for the sequences considered, the results indicate that the integrated and averaged variables are not significantly altered for the current level of fuel modeling, however, the localized variables such as nodal temperature and oxide thickness are affected.

I. INTRODUCTION

The exothermic reaction of zirconium and its alloys with steam can add large amounts of heat to the nuclear decay heat of a severely undercooled core (6.43 MJ/kg of zircaloy reacted). Also, the hydrogen reaction product, which is eventually released to the containment building, can present a sizable threat to containment integrity. These considerations necessitate a thorough understanding of the Zircaloy oxidation reaction and accurate mathematical modeling of this reaction for use in analyzing various potential accident sequences. To this end, an improved Zircaloy oxidation model has been developed and incorporated into the MARCH 2 (Meltdown Accident Response Characteristics) code (1).

The rate of Zircaloy oxidation in a degraded undercooled core can be controlled by several physical processes assuming steam is available to react. These physical processes can be grouped into three broad classifications of physical phenomena:

1) Solid-state processes (clad, channel box, etc.),
2) Gas phase transport (coolant channel), and
3) Zirconium oxide (ZrO_2)/gas interface interaction.

The latter phenomenon was not modeled in the MARCH 1.1 code (2). The rate of clad oxidation in MARCH 1.1 was taken to be the slower of the solid-state or gaseous diffusion rates. The user was given the option of choosing the Cathcart (3) or Baker-Just (4) model for solid-state diffusion, and gaseous diffusion was modeled according to Baker-Just (4).

Several of the processes included in the three classifications of physical phenomena listed above will now be enumerated. Depending on the flow regime, gas phase transport processes include the diffusion of steam through a steam/hydrogen mixture in laminar flow to the ZrO_2 surface (with counter-current flow of hydrogen) as well as possible mixing due to turbulent flow conditions. The ZrO_2/gas interface interactions include physical processes such as chemisorption of steam, dissociation of the steam on the surface into oxygen and hydrogen, hydrogen recombination, and finally desorption of the hydrogen from the ZrO_2 surface. The solid-state processes consist of diffusion of the oxygen anions through the anion deficient ZrO_2 lattice, through the oxygen stabilized α-Zr layer to the β-Zr interface, ZrO_2 phase transformations, and other physical processes such as the formation of porous and cracked oxides which can result in substantially higher oxidation rates than those encountered with the dense oxide layers.

An improved Zircaloy-steam reaction model, which accounts for several of the physical processes described above, has been incorporated into MARCH 2. Some of the features which have been included are:

1) Improved physical modeling for solid-state oxidation to account for the high temperature ZrO_2 phase transformation,
2) Improved geometric modeling for gaseous diffusion oxidation,
3) Chemisorption/dissociation retardation due to high hydrogen partial pressures,
4) Laminar and turbulent flow conditions, and
5) Automatic timestep contraction and expansion within a MARCH timestep.

Section II presents a brief summary of the previous Zircaloy oxidation model that is in the MARCH 1.1 code. In Sections II.A. and II.B. the new model features are derived, assumptions are discussed, and differences between the MARCH 1.1 and 2 versions are discussed. Section III presents a comparison of the MARCH 1.1 and MARCH 2 results. Finally, the summary and conclusions are presented in Section IV.

II. MODEL DEVELOPMENT

As mentioned in Section I, the solid-state oxidation rates available in MARCH 1.1 are those of Baker-Just and Cathcart. The Baker-Just relation can be written in the following form:

$$\left(\frac{dx}{dt}\right)_{ss} = \frac{10^{-6}K_p}{2.0\rho_{Zr}^2 x} = \frac{(0.3937)}{x}\exp\left(\frac{-45500.0}{R\,T_{fuel}}\right) \quad , \quad [1]$$

where

x = oxide layer thickness, (cm);

K_p = parabolic rate law constant, $((\text{mg Zr/cm}^2)^2/\text{sec})$;

R = gas constant, (1.987 cal/(mole)(K));

T_{fuel} = lumped fuel rod temperature, (K);

t = time, (sec); and

ρ_{Zr} = zirconium density, (6.5 g/cc).

Similarly, the Cathcart relation can be written in the following form:

$$\left(\frac{dx}{dt}\right)_{ss} = \frac{(0.0373)}{x}\exp\left(\frac{-39940.0}{R\,T_{fuel}}\right) \qquad [2]$$

Inherent in Equations [1] and [2] are assumptions of:

1) planar geometry,
2) the solid-state oxidation process is independent of steam and hydrogen concentration,
3) the microstructure does not change with temperature, and
4) the oxide layer remains intact (i.e., no cracking).

The gaseous diffusion oxidation rate available in MARCH 1.1 is that of Baker-Just:

$$\left(\frac{dx}{dt}\right)_{gd} = \frac{Nu\,D_o M_{Zr}}{2^{1.68}\rho_{Zr}\,n\,R}\frac{r_o}{r^2}(T_s + T_w)^{0.68}\left[\frac{p_s^b - p_s^c}{P_{tot}}\right]$$

$$\approx \frac{(5.636 \times 10^{-6}) r_o (T_{film})^{0.68}}{(r_o - x)^{2.0}}\left[\frac{p_s^b - p_s^c}{P_{tot}}\right]^{1.0}, \qquad [3]$$

where

Nu = Nusselt number ;

D_o = diffusion constant, $(6.25 \times 10^{-5}$ $(cm^2)(atm)/(sec)(K^{1.68}))$;

M_{Zr} = atomic weight of zirconium, (91.22 g/atom);

n = moles of hydrogen generated per atom metal reacted ;

r_o = fuel rod outer radius, (cm);

r = radius of unreacted metal, (cm);

T_s = oxide surface temperature, (K);

T_w = bulk water temperature, (K);

T_{film} = average of the rod and steam temperature, (K);

p_s^b = partial pressure of steam in the bulk stream ;

p_s^c = partial pressure of steam at the oxide-gas interface ; and

P_{tot} = total system pressure.

Equation [3] can be derived from the following general relation:

$$\left(\frac{dx}{dt}\right)_{gd} = \frac{N_g(t)\,M_{Zr}}{2.0\,\rho_{Zr}}, \qquad [4]$$

where

$N_g(t) = k_c(C_A - C_W)^{0.0}$

= mass flux due to gas phase transport ;

k_c = mass transfer coefficient, (cm/sec);

C_A = steam concentration in bulk stream ; and

C_W = steam concentration at the oxide-gas interface.

Thus in MARCH 1.1, the pressure dependence in the gaseous diffusion model is eliminated by assuming the concentration of steam and the partial pressure of hydrogen at the oxide-gas interface are zero.

Similarly, Equations [1] and [2] can be derived from the more general relation:

$$\left(\frac{dx}{dt}\right)_{ss} = \frac{N_s(t)\,M_{Zr}}{2.0\,\rho_{Zr}} f(P_h^c)^{1.0}, \qquad [5]$$

where

$N_s(t)$ = mass flux predicted by the parabolic rate law, and

$f(P_h^c)$ = experimentally determined function dependent on hydrogen partial pressure at the oxide-gas interface.

Therefore in MARCH 1.1 the hydrogen partial pressure impact at the oxide surface was ignored by assuming $f(P_h^c) = 1.0$. This assumption has been retained in the MARCH 2 model up to a ratio of hydrogen partial pressure to total pressure of 0.5. Also, the assumption that the partial pressure of steam at the oxide-gas interface is zero which was made in the MARCH 1.1 gaseous diffusion model deviation has been retained up to a fractional hydrogen pressure of 0.5. An improved physical model for the solid-state oxidation reaction and an improved geometric model (for conditions of laminar and turbulent flow) for gaseous diffusion oxidation have been adopted and these models are discussed in Section II.A. The assumptions made in Equations [4] and [5] will be relaxed for fractional hydrogen pressures in excess of 0.5 and pressure dependent terms utilized in place of constants for C_w and $f(P_h^c)$.

II.A. Steam-Rich Environment

The solid-state oxidation model adopted is that of Urbanic-Heidrick (5). As shown experimentally in Reference (5), steam reacts with β-Zr to form a layer of oxygen-stabilized α-Zr as well as a surface layer of ZrO_2. Urbanic and Heidrick measured the rate of growth of the (ZrO_2 + α-Zr) layer and the reaction kinetics of Zircaloy-2 and Zircaloy-4 in steam. They found that the reaction in both alloys obeyed parabolic kinetics, and there was a discontinuity in the temperature dependence of the reaction rate near 1577 C. This discontinuity was explained by reference to the zirconium-oxygen phase diagram. Above 1577 C, the oxide structure changes from predominantly tetragonal ZrO_2 to (tetragonal ZrO_2 + cubic ZrO_2) as shown in Figure 1 (6). The coincidence of the discontinuity in the temperature dependence of the reaction rate observed by Urbanic-Heidrick at 1580 C and the phase transformation is striking. Similar observations were reported by Pemseler (7) for the activation energy change for oxide growth on zirconium at 900 C. He attributed the change to the monoclinic/tetragonal transformation of ZrO_2. Urbanic and Heidrick offered no further explanation regarding the detailed mechanisms involved in the dramatic increase in the oxidation rate at 1577 C. If we accept the fact that the

phase transformation is indeed the triggering mechanism, then the cause for increased oxidation rate can be attributed to either enhanced diffusion in the more open cubic lattice or oxide cracking due to the phase change induced stresses. The volume change associated with the tetragonal to cubic transformation results in approximately a 1.5% increase in volume. However, since the rate constant versus 1/T curve does not change slope substantially after the phase change as illustrated in Figure 2, it is likely that the mechanism of transport is not substantially altered (i.e., similar activation energy). Therefore, it is likely that the rate increase is due primarily to enhanced diffusion in the cubic lattice. Unfortunately, there is no data on diffusion in ZrO_2 above 1200 C and the resolution of the question will have to be the subject of future research.

The Baker-Just, Cathcart, Urbanic-Heidrick, and Ianni (8) parabolic rate constants are plotted versus reciprocal temperature for comparison in Figure 2. The Baker-Just reaction rates are observed to conservatively bound the other reaction rate results. This is because they studied the reaction in the temperature range of 1100-4000 C. Their rate law was extrapolated to low temperature. The Urbanic-Heidrick results agree fairly well with Baker-Just above 1577 C. Cathcart studied the zircaloy oxidation reaction in the temperature range of 900-1500 C. The Urbanic-Heidrick results agree fairly well with the Cathcart results up to 1577 C. In MARCH 1.1, the Cathcart reaction rate is extrapolated above 1577 C. Also shown in Figure 2 for interest is Ianni's model. Based on Pemseler's observation of a change in the activation energy at 900 C due to the allotropic transformation of monoclinic ZrO_2 to tetragonal ZrO_2, Ianni anticipated changes in slope of the parabolic rate constant versus inverse temperature plot at the two allotropic transformation temperatures, and he reported three separated expressions to describe the Zircaloy-2/steam reaction from room temperature to the melting point of Zircaloy-2. Ianni's results in Figure 2 were obtained by replotting the Baker-Just data at the melting point and using Lemmons (9) data in the temperature range of 1000-1577 C.

The Urbanic-Heidrick solid-state reaction rate equations incorporated into MARCH 2 are as follows:

$T_{fuel} \leq 1577$ C

$$\left(\frac{dx}{dt}\right)_{ss} = \frac{(3.5030 \times 10^{-3})}{x} \exp\left(\frac{-16820.0}{T_{fuel}}\right) \qquad [6]$$

$T_{fuel} > 1577$ C

$$\left(\frac{dx}{dt}\right)_{ss} = \frac{(1.0402 \times 10^{-2})}{x} \exp\left(\frac{-16610.0}{T_{fuel}}\right) \qquad [7]$$

The gas phase diffusion model adopted for laminar flow is that developed by Walters and Genco during the NURLOC-1.0 study (10). Equation [4] was used with $C_W = 0.0$. The mass transfer coefficient used in NURLOC-1.0 is given by:

$$Nu'_{de}(z) = \frac{k_c(z)\, de}{D_v} = a\left(\frac{s}{r_o}, \varepsilon\right)[4.36 + g(z, N_R, N_{sc})] \quad , \qquad [8]$$

where

$$g(z, N_R, N_{sc}) = \frac{0.036\left[\frac{N_R N_{sc}\, de}{z}\right]}{1.0 + 0.0011\left[\frac{N_R N_{sc}\, de}{z}\right]} \quad ,$$

$$a\left(\frac{s}{r_o}, \varepsilon\right) = \frac{q\left(\frac{s}{r_o}\right)}{4.36} \frac{(f/2)_s}{(f/2)_t} \frac{de}{d} \quad ,$$

$Nu'_{de}(z)$ = local Nusselt number for mass transfer ,

$k_c(z)$ = axially dependent mass transfer coefficient ,

D_v = diffusivity of steam through hydrogen ,

$N_{sc} = \frac{\mu}{\rho D_v}$ = Schmidt number ,

z = axial position ,

de = equivalent diameter ,

N_R = Reynolds number ,

s = center-to-center distance of cylinders ,

$q\left(\frac{s}{r_o}\right)$ = Nusselt number in triangular array tube bundle ,

$(f/2)_s$ = friction factor based on a square array, fully developed flow , and

$(f/2)_t$ = friction factor based on a triangular array, fully developed flow .

Equation [8] combined the work of Kays (11) on heat transfer during boundary layer development, and that of Sparrow (12,13) on the fully developed laminar flow region. The equation is valid for a square array of fuel rods. Figure 3 is a schematic diagram of the model. As illustrated, a mixture of hydrogen and steam is assumed to flow at a velocity (V) through a rectangular annulus about a fuel rod. The steam which reacts with the fuel rod results in a flux density of steam $N_A(t)$.

The Nusselt number in a triangular array tube bundle is linearily approximated as shown in Figure 4. The linear relation used in the code is:

$$a\left(\frac{s}{r_o}\right) = -1.5060\left(\frac{s}{r_o}\right) + 7.05 \qquad [9]$$

The friction factor-Reynolds number relationship as a function of the porosity for tube bundles is illustrated in Figure 5. These functions were multilinearized as shown and the coded equations are:

$\varepsilon > 0.7$

$$\frac{f_s}{f_t} = 1.0 \qquad [10]$$

$0.494 \leq \varepsilon \leq 0.7$

$$f_s = (-41.0714)\,\varepsilon + 42.8893$$
$$f_t = (-67.8571)\,\varepsilon + 61.5214 \qquad [11]$$

$\varepsilon < 0.494$

$$f_s = (-29.1498)\,\varepsilon + 37.0$$
$$f_t = (-130.8140)\,\varepsilon + 92.6221 \qquad [12]$$

In summary, the gaseous diffusion oxidation rate for laminar flow in a square array is given by:

$$\left(\frac{dx}{dt}\right)_{gd} = (1.6468 \times 10^{-6})(T_{film})^{0.68} g(z, N_R, N_{sc})$$

$$a\left(\frac{s}{r_o}, \varepsilon\right) \left[\frac{P_s^b - P_s^c}{P_{tot}}\right]^{0.0} \quad . \qquad [13]$$

As illustrated schematically in Equation [13], the steam pressure at the oxide-gas interface is taken to be zero. In effect, it is assumed that all of the steam which reaches the oxide surface reacts.

For the case of gaseous diffusion oxidation in turbulent flow, a modified Dittus-Boelter relation was developed. The heat-mass transfer analogy was employed to obtain the following relationship for turbulent mass transfer:

$$k_c = \frac{D_v(0.0230)\, N_R^{0.8}\, N_{sc}^{0.4}}{de} \quad . \qquad [14]$$

The oxidation rate is therefore given by:

$$\left(\frac{dx}{dt}\right)_{gd} = (1.2800 \times 10^{-7}) N_R^{0.8}\, N_{sc}^{0.4} \left[\frac{P_s^b - P_s^c}{P_{tot}}\right]^{0.0} \qquad [15]$$

As assumed in Equation [13], the steam partial pressure at the oxide-gas interface is taken to be zero. This assumption is made for hydrogen partial pressure to total pressure ratios less than 0.5. The reasoning behind this choice of hydrogen partial pressure to total system pressure ratio cutoff will be discussed further in Section II.B.

The effect of non-planar geometry on the solid-state oxidation rate was not accounted for in the MARCH 1.1 or improved model. In cylindrical geometry, diffusion through the ZrO_2 layer depends not only on the oxide thickness, but also on the ratio of the ZrO_2/β-Zr interface radius to the outer radius. As shown in Table 1, this effect can result in a 6.0-7.0% higher oxidation rate than that predicted for a planar geometry model. Table 1 was calculated using the relations found in Appendix B of Reference (4).

TABLE 1. NON-PLANAR GEOMETRY EFFECTS ON OXIDATION RATE FOR TYPICAL LWR FUEL ROD

Percent of Clad Reacted	Cylindrical Geometry Rate / Planar Geometry Rate
0	0.0
20	1.011
40	1.023
60	1.035
80	1.049
100	1.063

II.B. Steam-Deprived Environment

High local hydrogen fractions can interfere with the steam diffusion to the ZrO_2 surface and the chemisorption/dissociation process at the solid/gas interface. A new model which accounts for the chemisorption/dissociation process and steam diffusion retardation due to high hydrogen partial pressures has been developed. Recent experiments (14) have shown that the solid-state oxidation rate can be significantly reduced in the presence of hydrogen when the ratio of hydrogen partial pressure to total pressure exceeds 0.5. Earlier research (3,15) indicated that there was no significant effect on the oxidation rate for hydrogen volume fractions less than approximately 0.3, which is consistent with the observations of Chung-Thomas (14).

The Reference (14) data were used to fit the mathematical model derived to describe this process as shown in Figure 6. Since the data are preliminary in nature, a simple linear relationship for the solid-state oxidation rate as a function of the fractional hydrogen pressure ratio in excess of 0.5 was assumed rather than a precise fit to the data. The linear approximation captures the physical phenomena reasonably well, and the model can be readily updated later as the data base expands. The chemisorption/dissociation process retardation was modeled as described and combined with the Urbanic-Heidrick equations to yield the following rate relationships:

$P_h^b > 0.5$ and $T_{fuel} \leq 1577$ C

$$\left(\frac{dx}{dt}\right)_{ss} = \frac{(3.5030 \times 10^{-3})}{x} \exp\left(\frac{-16820.0}{T_{fuel}}\right)\left[\frac{P_s^b}{P_{tot}}\right] \qquad [16]$$

$P_h^b > 0.5$ and $T_{fuel} > 1577$ C

$$\left(\frac{dx}{dt}\right)_{ss} = \frac{(1.0402 \times 10^{-2})}{x} \exp\left(\frac{-16610.0}{T_{fuel}}\right)\left[\frac{P_s^b}{P_{tot}}\right] \qquad [17]$$

where

P_s^b = hydrogen partial pressure in bulk steam.

The new MARCH 2 solid-state oxidation rate is compared with the MARCH 1.1 model in Figure 7. Obviously, there is a substantial difference in the predicted oxidation rate for $P_h^b/P_{tot} > 0.5$.

For the case of gaseous diffusion limited oxidation, the steam pressure at the oxide-gas interface was assumed to be given by:

$$P_s^c = \left(\frac{P_h^b}{P_{tot}}\right) P_s^b \quad . \qquad [18]$$

Therefore, the rate equation for laminar flow is given by:

$$\frac{p^b_h}{P_{tot}} > 0.5$$

$$\left(\frac{dx}{dt}\right)_{gd} = \frac{(1.6468 \times 10^{-6})(T_{film})^{0.68}}{r_o} g(z,N_R,N_{sc})$$

$$a\left(\frac{s}{r_o}, \varepsilon\right)\left[\frac{p^b_s p_{tot} - p^b_h p^b_s}{p^{2.0}_{tot}}\right] \qquad [19]$$

The rate equation for turbulent flow is given by:

$$\frac{p^b_h}{P_{tot}} > 0.5$$

$$\left(\frac{dx}{dt}\right)_{gd} = (1.2800 \times 10^{-7}) Re^{0.8} N_{sc}^{0.4} \left[\frac{p^b_s p_{tot} - p^b_h p^b_s}{p^{2.0}_{tot}}\right] \qquad [20]$$

Unfortunately, data are lacking to verify the assumption in Equation [18]. As the data base expands, this function can be easily modified to take higher order effects into account for the gaseous diffusion models. The MARCH 2 gaseous diffusion model is also compared with the MARCH 1.1 model in Figure 7. At each nodal location in the core, the code analyzes the flow regime and the limiting appropriate oxidation rate equation is employed.

Another model feature which has been incorporated into the code is the automatic timestep reduction and expansion algorithm. In general, the gaseous diffusion oxidation rates are quite high, and therefore a very small timestep is required (~ milliseconds). For fresh fuel with very little or no protective oxide thickness, the gaseous diffusion oxidation is the limiting rate. After several timesteps (as the oxide thickness increases), the solid-state oxidation rate becomes the limiting rate, and a larger timestep (~ seconds) can then be used. The new algorithm reduces the MARCH timestep substantially when gaseous diffusion rates limit, and expands back to a larger timestep when the solid-state oxidation rates limit. When solid-state oxidation is the rate limiting process, the MARCH timestep is reduced by a factor of two until the thickness of clad oxidized in one timestep is less than approximately 0.1 percent of the unreacted thickness. It is anticipated that this algorithm will be useful in advanced fuel models which account for the oxidation of fresh clad surface due to fuel melting and/or clad rupture in advanced stages of an accident.

III. COMPARISON OF CODE RESULTS

The T (transient event) M (failure of secondary system steam relief valves and power conversion system) L (failure of secondary system steam relief valves and auxiliary feedwater system) B (failure of electric power to engineered safety features) sequence was run for a Pressurized Water Reactor (PWR) with a large dry containment. The integrated and averaged results for several parameters and the timing of key events are presented in Table 2. In this case, the Zircaloy was allowed to oxidize after the fuel became molten. The oxidation rate laws were linearly extrapolated at high temperatures when the Zircaloy becomes molten. This assumption should be the subject of future research since there is currently little data to substantiate the assumed extrapolation. As observed in Table 2, there are negligible differences in the timing of key events and in core averaged and integrated parameters such as the total fraction of clad reacted. An oxide thickness of 1.0×10^{-4} cm was assumed to exist on the clad outside surface at the start of the accident. This thickness was obtained from the corrosion data of Harrop, et al (15), for Zircaloy-2 in water at 300 C for 1000 hours. For initial oxide thicknesses of this magnitude, the solid-state oxidation is the limiting rate and the gaseous diffusion model is not utilized. Therefore, the results of Table 2 are a comparison of the solid-state oxidation model results. The reason that the Baker-Just model predicts a slightly larger

TABLE 2. EFFECT OF ZIRCALOY OXIDATION MODEL IN PWR LARGE DRY CONTAINMENT - TMLB SEQUENCE

Event	Improved Model[a]	Cathcart Solid-State Baker-Just Gaseous Diffusion	Baker-Just Solid-State Baker-Just Gaseous Diffusion
Core Uncovery (min)	73	73	73
Melt Initiation (min)	90	90	89
Core Slump (min)	119	119	117
fraction clad reacted	0.584	0.580	0.605
debris temperature (K)	3733	3678	3747
Head Failure (min)	126	125	124
fraction clad reacted	0.713	0.695	0.739
debris temperature (K)	2609	2574	2618
total hydrogen (kg)	627	611	650

(a) 10 radial nodes and 24 axial nodes

fraction of clad reacted than the Cathcart model can be readily explained by reference to Figure 2. At temperatures above approximately 1000 C, the Baker-Just oxidation rate significantly exceeds the Cathcart rate. The improved model predicts a comparable fraction of clad reacted. As mentioned in Section II, this model accounts for the ZrO_2 phase change as well as hydrogen overpressure effects. The hydrogen overpressure condition was observed to occur for only a few minutes during the accident, and as a result, the effect of this phenomenon is of minor importance to the integrated and averaged core variables. The impact of these modeling features on localized variables such as nodal temperature and oxide thickness will be discussed later in this section.

In order to investigate the hydrogen overpressure impact further, a modified TML sequence was analyzed for a PWR with a large dry containment using the improved model with and without the hydrogen overpressure feature. The Emergency Core Cooling System (ECCS) was assumed to be partially degraded and the flow rate for the high head pumps was adjusted so that after core uncovery the liquid level was maintained at 60 cm above the bottom of the active fuel. This sequence was run in an attempt to create a situation where the hydrogen overpressure condition would prevail for longer periods of time than in the TMLB sequence. The clad oxidation was purposely suppressed when melting occurred so that the fuel heatup behavior could be studied. The results for this sequence are presented in Table 3 and also in Figures 8, 9, and 10. Once again, the core averaged and integrated parameters did not differ significantly for the models compared. However, locally there were differences in several key variables such as nodal temperature, oxide thickness, and clad melt timing and location. Figure 10 illustrates the localized effect of the hydrogen overpressure model on the oxidation rate and the time to fuel melting. The results are shown for an outer radial node at an axial height of 244.0 cm from the bottom of the active fuel.

The oxide thickness axial profile for the modified TML sequence at the central radial node is shown in Figure 11 along with the axial core power profile. This distribution is plotted at 87 minutes which is the timestep just prior to fuel melting. The peak oxide thickness (which occurs at an axial height in the range of 250.0-260.0 cm for the three cases analyzed) is driven by the axial core power distribution, the water height (60.0 cm), the core uncovery rate, axial conduction, and the steam/hydrogen heat transfer at this time in the accident. At an axial height of approximately 195.0 cm, the Cathcart and improved model results cross as shown in Figure 11. This is due to the fact that the Cathcart solid-state reaction rate is higher than the Urbanic-Heidrick rate at temperatures in the range of 1150-1577 C as shown in Figure 2. The oxide thickness axial profiles just prior to core collapse into the lower plenum for the central radial node and an outer radial node are shown in Figures 12 and 13, respectively. As shown in Figure 12, the oxide axial profiles at core collapse are significantly changed from those plotted at 87 minutes. At this time in the accident, the oxide profile redistribution is driven by hydrogen overpressure, steam starvation, slumping model assumptions, core power distribution, water level, steam/hydrogen heat transfer, and axial conduction. In all the cases reported herein, MARCH meltdown model A was implemented. In this model the heat in excess of that required to keep a node molten is transferred downward. As illustrated by the similarity in shape and magnitude of Curves 1 and 3 in Figure 12, there is little effect due to hydrogen overpressure at the central radial node because of the rapid heatup and melting. However, there are substantial changes in the axial oxide profile due to the hydrogen overpressure effect in the outer radial region as shown in Figure 13. The hydrogen overpressure also affects the axial height at which clad melting occurs as illustrated in Figure 13.

The oxide thickness axial profiles for the TMLB sequence were also analyzed for the improved, Cathcart, and Baker-Just models. The improved model and the Baker-Just model predict clad melting at approximately the same axial height, whereas the Cathcart prediction is about 30.0 cm higher in the core. The axial distribution plotted in Figure 14 is for 115 minutes for the central radial node. As illustrated, the Baker-Just model prediction of the oxide thickness is substantially higher than the Cathcart or improved model predictions. Once again, this is explained by reference to Figure 2. It is interesting to compare Figures 12 and 14 and note

TABLE 3. EFFECT OF ZIRCALOY OXIDATION MODEL IN PWR LARGE DRY CONTAINMENT - MODIFIED TML SEQUENCE

Event	Improved Model(a)	Improved Model(b)	Cathcart Solid-State Baker-Just Gaseous Diffusion	Improved Model (No H_2 Overpressure)
Core Uncovery (min)	72	72	72	72
Melt Initiation (min)	88	88	88	88
Core Slump (min)	105	105	105	107
fraction clad reacted	0.383	0.399	0.414	0.397
debris temperature (K)	2544	2504	2517	2523
Head Failure (min)	117	116	116	118
debris temperature (K)	1787	1763	1772	1774
total hydrogen (kg)	335	349	362	347

(a) 10 radial nodes and 48 axial nodes
(b) 10 radial nodes and 24 axial nodes

the differences in the oxide axial profiles for the cases of boildown to a constant water level and boil dry.

An analysis was performed to assess the impact of the choice of axial mesh on the improved oxidation model. Twenty-four axial nodes and ten radial nodes were used in the results reported in Figures 11-14. The modified TML sequence was rerun with 48 axial nodes and ten radial nodes. The results are presented in Table 3 and Figure 15. The 480 node run predicts 4.0% lower total fraction of clad reacted than the 240 node mesh using the same axial power profile. Also, there are changes in the oxide thickness axial profiles as shown in Figure 15. The 240 node mesh improved model results shown in Figure 11 are replotted along with the 480 node mesh. At later times in the accident, oscillations were observed in the thickness of the oxide along the axis of the fuel rod. This is believed to be the result of the non-mechanistic nature of meltdown model A and the smaller heat capacity of each node in the case of the refined mesh.

The fuel is not likely to fail under its own weight since the stresses are quite low. The most likely failure mechanisms are failure due to pressure loads (ballooning, overstressing, etc.) or Zircaloy melting with either ZrO_2 cracking or subsequent ZrO_2 melting. MARCH is currently capable of modeling fuel failure by melting only. As illustrated in Figures 12-14, the improved model predicts clad melting within approximately 30.0 cm of the MARCH 1.1 model prediction. This difference is insignificant when weighed against other modeling assumptions and uncertainties. The nodal temperatures were also plotted as a function of time at several axial locations for the improved, Cathcart, and Baker-Just models. The differences in the temperature profiles for the three models is not large. Therefore, there is no reason to believe that the improved oxidation model has a significant impact on fission product release and transport. As the level of detail in fuel modeling increases and knowledge of severe accident phenomenology improves, this preliminary indication may change.

IV. SUMMARY AND CONCLUSIONS

- An improved Zircaloy-steam oxidation reaction model has been incorporated into the MARCH 2 code.
- The integrated and averaged variables are not significantly changed using the improved model for the current level of fuel modeling in MARCH for the sequences analyzed. This conclusion may change in the future as knowledge regarding severe accident phenomenology increases and more advanced fuel models are developed to account for fuel heatup and relocation more mechanistically.
- Localized variables, such as nodal temperature and oxide thickness, are affected using the improved model for the sequences analyzed. These effects are more significant in the outer radial regions of the core where heatup is more gradual and the hydrogen partial pressure to total pressure ratio is in excess of 0.5 for longer periods of time.
- The overall effect of the hydrogen overpressure model in a degraded uncovered core that is steam limited is to attenuate the oxidation reaction and redistribute more steam (and therefore greater oxide thickness) to the upper axial regions of the core.
- The impact of the improved oxidation model on fuel failure location and hence fission product release and transport is judged to be negligible for the sequences analyzed. However, this conclusion may change in the future as more advanced fuel models are developed.

V. ACKNOWLEDGEMENTS

I wish to acknowledge and thank the U.S. Nuclear Regulatory Commission and Sandia National Laboratories for the sponsorship of this research. I also wish to thank my colleagues Dr. R. S. Denning, Dr. J. C. Cunnane, Mr. P. Cybulskis, Mr. R. O. Wooton, and Miss A. E. Browning for many fruitful discussions and helpful suggestions throughout the research. I also wish to thank Ms. L. L. Judd for the timely and impeccable preparation of the final manuscript.

Finally, I wish to thank my dedicated wife, Georgina, and beautiful baby, Jennifer, for sacrificing our time together to allow me to prepare this manuscript. Thanks, girls!

REFERENCES

(1) Cybulskis, P., Wooton, R. O., and Denning, R. S., "Development of MARCH 2", Proceedings of the International Meeting on Thermal Reactor Safety, held at Chicago, IL, August 29-September 2, 1982, NUREG/CP-0027, Vol. 2, pp 1158-1166.

(2) Wooton, R. O., and Avci, H. I., "MARCH 1.1 (Meltdown Accident Response Characteristics) Code Description and User's Manual", NUREG/CR-1711 (October, 1980).

(3) Cathcart, J. V., "Quarterly Progress Report on the Zirconium Metal-Water Oxidation Kinetics Program Sponsored by the NRC Division of Reactor Safety Research for October-December, 1976", Oak Ridge National Laboratory, ORNL/NUREG/TM-87.

(4) Baker, L., and Just, C., "Studies of Metal-Water Reactions at High Temperatures III. Experimental and Theoretical Studies of the Zirconium-Water Reaction", Argonne National Laboratory, ANL-6548 (May, 1962).

(5) Urbanic, V. F., and Heidrick, T. R., "High-Temperature Oxidation of Zircaloy-2 and Zircaloy-4 in Steam", Journal of Nuclear Materials, 75 (1978).

(6) Elliot, R. P., "Constitution of Binary Alloys", First Supplement McGraw-Hill, New York (1965).

(7) Pemsler, J. P., "The Kinetics and Mechanism of Oxide Film Growth of Zirconium", Electrochemical Technology, 4(3-4), pp 128-131 (1966).

(8) Ianni, P. W., "Metal-Water Reactions: Effects on Core Cooling and Containment", APED-5454, General Electric Co., San Jose, CA (1968).

(9) Lemmon, A. W., "Studies Relating to the Reaction Between Zirconium and Water at High Temperatures", BMI-1154, Battelle Memorial Institute, Columbus, OH (1957).

(10) Walters, C. T., and Genco, J. M., "A Digital Computer Program for Thermal Analysis of a Nuclear Reactor Loss-of-Coolant Accident", AEC Contract No. W-7504-ENG-92 (1967).

(11) Kays, W. M., "Numerical Solution for Laminar-Flow Heat Transfer in Circular Tubes", Transactions of ASME, 77, p 1265 (1955).

(12) Sparrow, E. M., Loeffler, A. L., and Hubbard, H. A., "Heat Transfer to Longitudinal Laminar Flow Between Cylinders", Transactions of ASME, 83, p 415 (1961).

(13) Sparrow, E. M., and Loeffler, A. L., "Longitudinal Laminar Flow Between Cylinders Arranged in Regular Array", AIChE Journal, 5, p 325 (1959).

(14) Chung, H. M., and Thomas, G. R., "The Retarding Effect of Hydrogen on Zircaloy Oxidation", NSAC-29, Interim Report (July, 1981).

(15) Harrop, P. J., Wilkins, W. J. M., and Wanklyn, J. W., "The Effect of Gamma Dose on Oxide Films of Zirconium and Zircaloy-2 and Its Relevance to Corrosion", Journal of Nuclear Materials, 16, pp 290-297 (1965).

(16) Homma, K., Furuta, T., and Kawasaki, S., "Behavior of Zircaloy Cladding Tube in a Mixed Gas of Hydrogen and Steam", JAERI-7131, Japan Atomic Energy Research Institute (December, 1977).

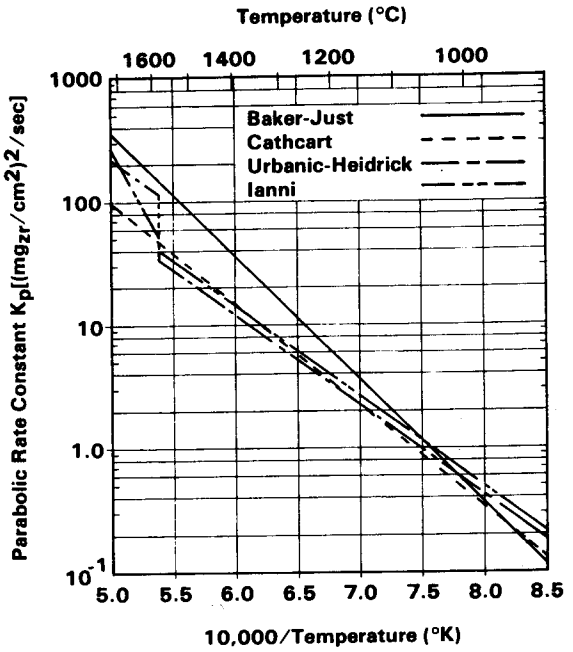

FIGURE 2. ZIRCALOY REACTION RATE IN STEAM

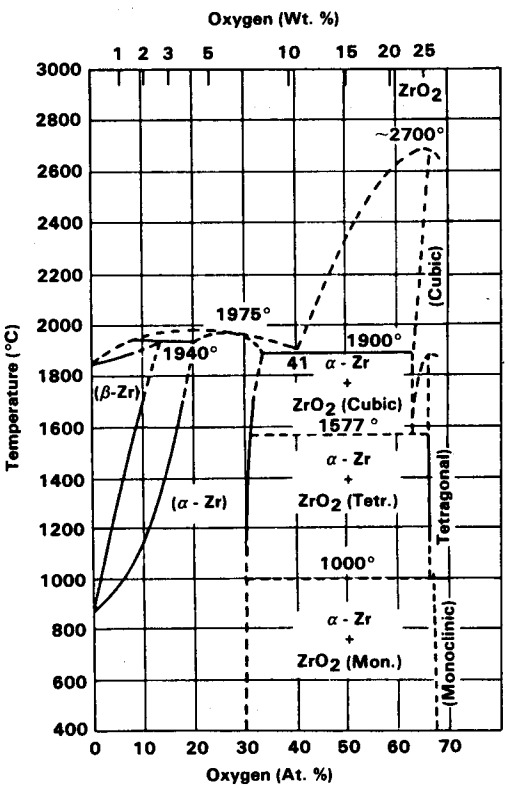

FIGURE 1. ZIRCONIUM-OXYGEN SYSTEM (FROM REF. 6)

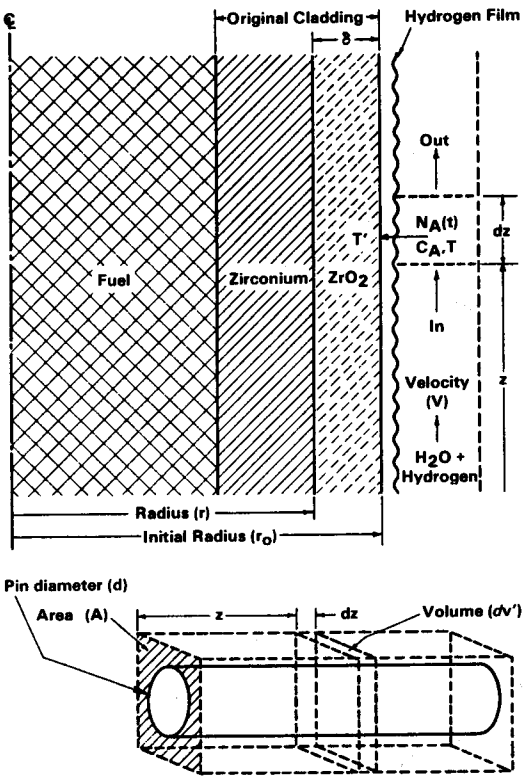

FIGURE 3. SCHEMATIC REPRESENTATION OF GASEOUS-DIFFUSION OXIDATION MODEL (FROM REF. 10)

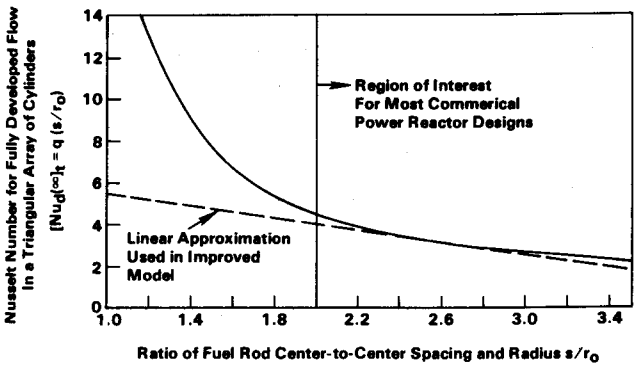

FIGURE 4. NUSSELT NUMBERS IN TRIANGULAR ARRAY TUBE BUNDLES (FULLY ESTABLISHED PARABOLIC VELOCITY PROFILE) (FROM REF. 10)

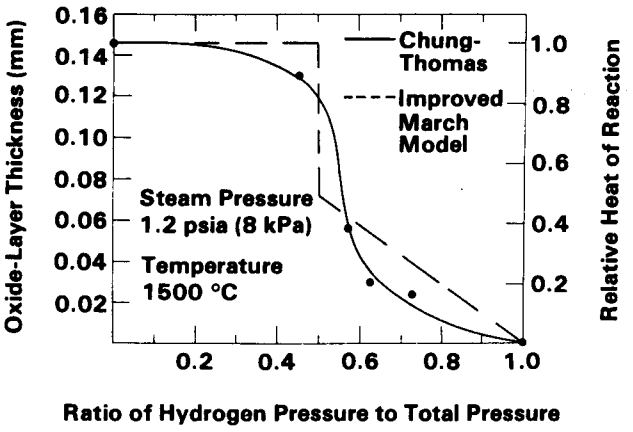

FIGURE 6. OXIDE-LAYER THICKNESS AFTER OXIDATION OF ZIRCALOY-4 FOR 200 SECONDS AT 1500 C AND A CONSTANT STEAM PRESSURE OF 8 KPa AS A FUNCTION OF FRACTIONAL HYDROGEN PRESSURE. ALSO SHOWN IS A NEW MODEL PREDICTION OF THE DATA ASSUMING OXIDATION RATE FOR HYDROGEN PARTIAL PRESSURE OF 0.0 IS THE SAME FOR THE MODEL AND EXPERIMENT (FROM REF. 14)

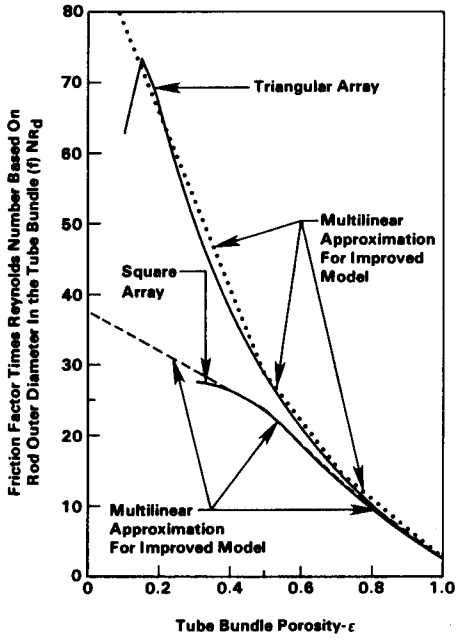

FIGURE 5. FRICTION FACTOR-REYNOLDS NUMBER RELATIONSHIP AS A FUNCTION OF POROSITY FOR TUBE BUNDLES (FROM REF. 13)

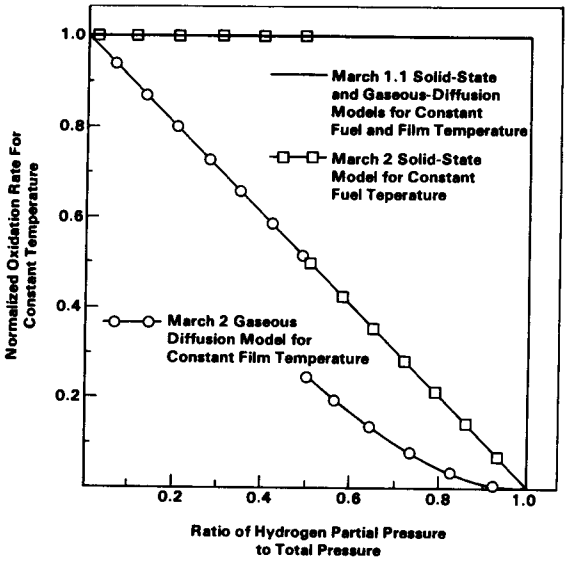

FIGURE 7. NORMALIZED OXIDATION RATE AS A FUNCTION OF FRACTIONAL HYDROGEN PRESSURE. THE MARCH 1.1 AND MARCH 2 MODEL PREDICTIVE CAPABILITY ARE COMPARED.

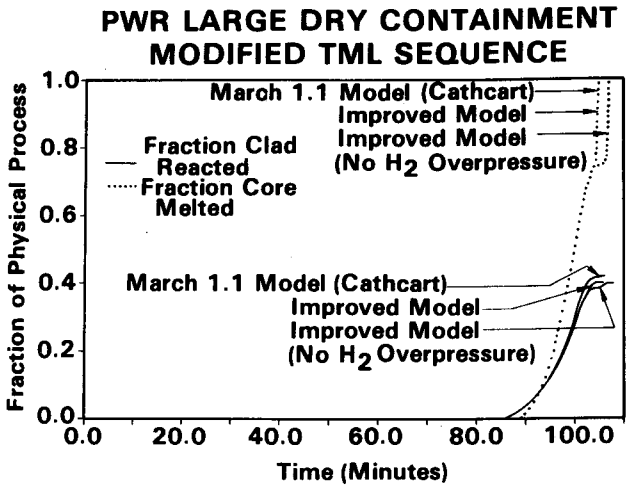

FIGURE 8. COMPARISON OF MACROSCOPIC VARIABLE RESULTS USING CATHCART SOLID-STATE AND IMPROVED ZIRCALOY OXIDATION MODELS

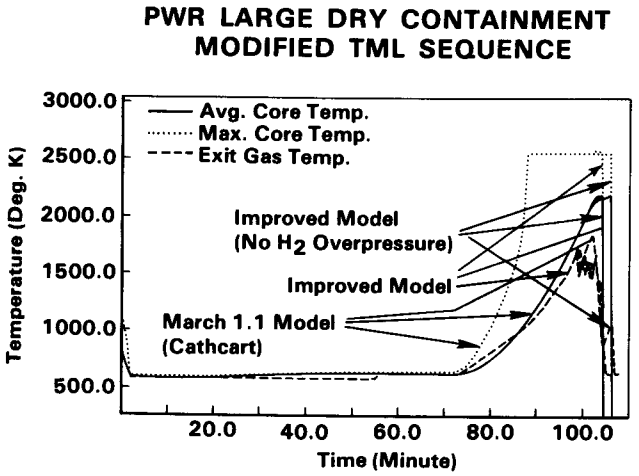

FIGURE 9. COMPARISON OF CORE TEMPERATURE RESULTS USING CATHCART SOLID-STATE AND IMPROVED ZIRCALOY OXIDATION MODELS

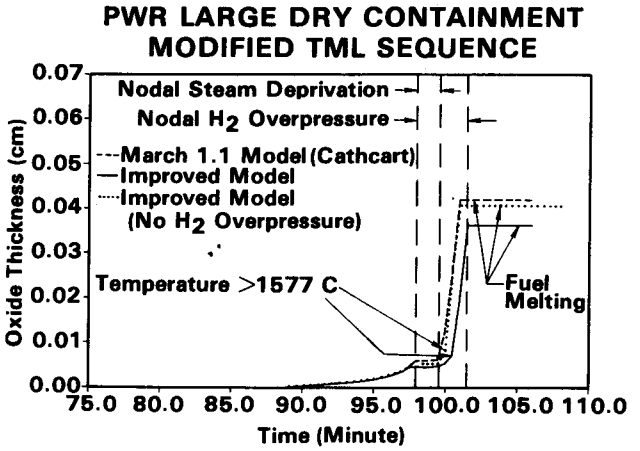

FIGURE 10. COMPARISON OF LOCAL VARIABLE RESULTS USING CATHCART SOLID-STATE AND IMPROVED ZIRCALOY OXIDATION MODELS. RESULTS SHOWN ARE FOR AN OUTER CORE RADIAL NODE AT 244.0 CM FROM THE BOTTOM OF THE ACTIVE FUEL.

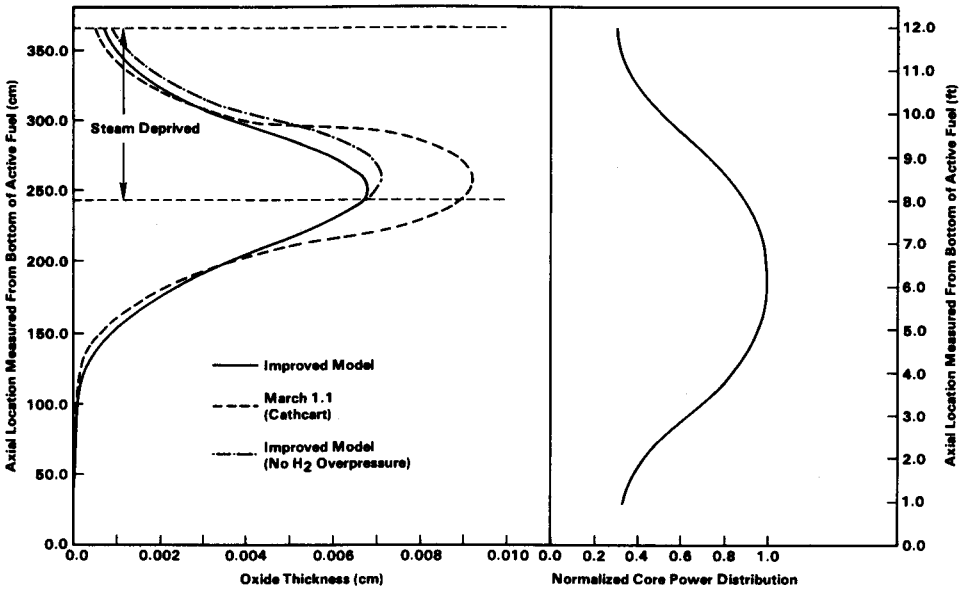

FIGURE 11. OXIDE THICKNESS AXIAL PROFILE IN THE CENTRAL RADIAL NODE FOR THE MODIFIED TML SEQUENCE AT 87 MINUTES (JUST PRIOR TO FUEL MELTING)

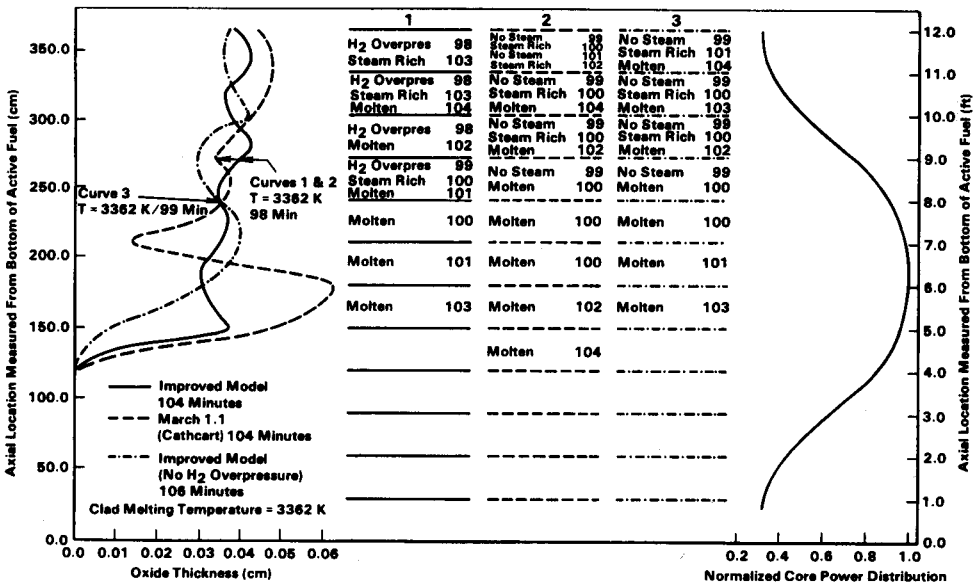

FIGURE 12. OXIDE THICKNESS AXIAL PROFILE IN THE CENTRAL RADIAL NODE FOR MODIFIED TML SEQUENCE JUST PRIOR TO CORE COLLAPSE INTO LOWER PLENUM

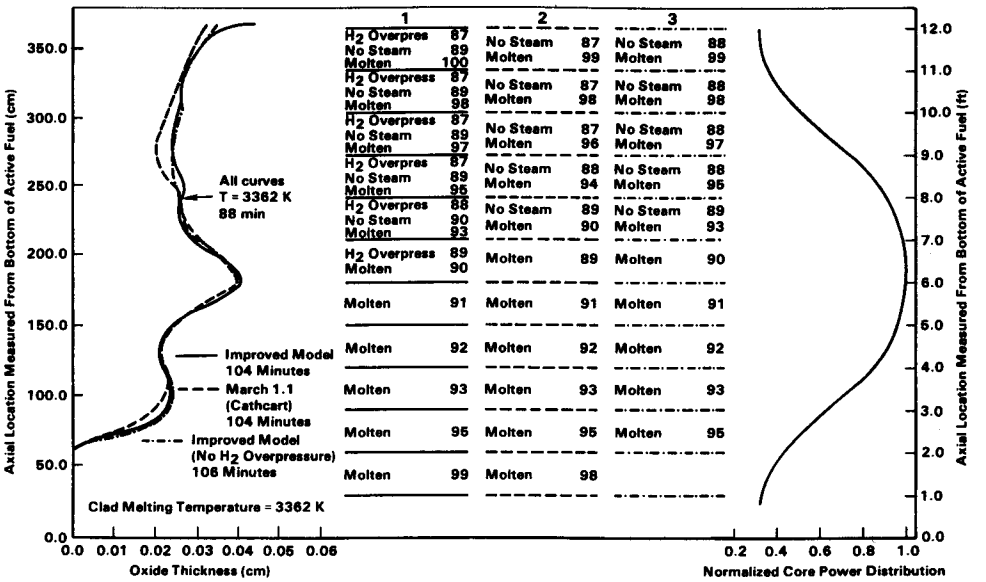

FIGURE 13. OXIDE THICKNESS AXIAL PROFILE IN AN OUTER RADIAL NODE FOR MODIFIED TML SEQUENCE JUST PRIOR TO CORE COLLAPSE INTO LOWER PLENUM

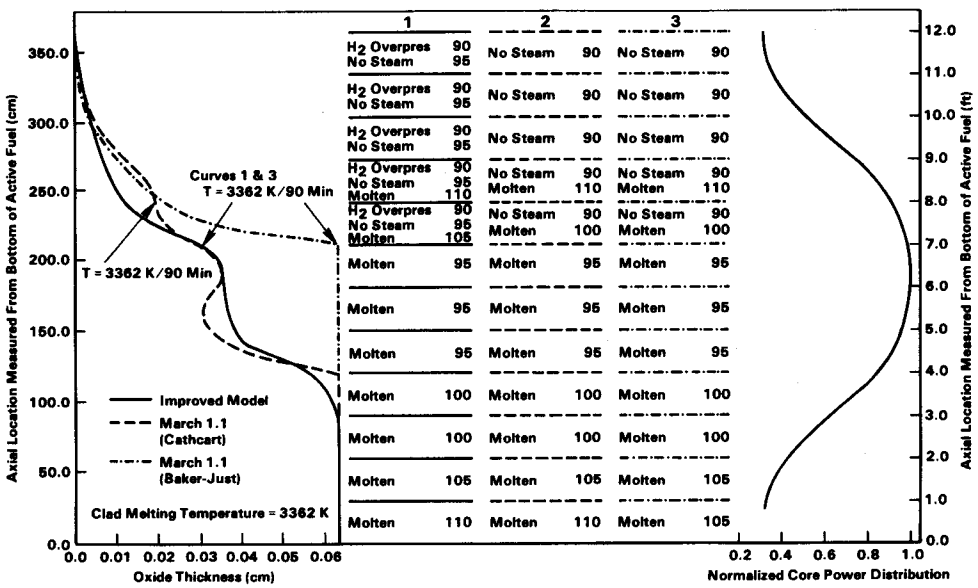

FIGURE 14. OXIDE THICKNESS AXIAL PROFILE IN THE CENTRAL RADIAL NODE FOR THE TMLB SEQUENCE AT 115 MINUTES

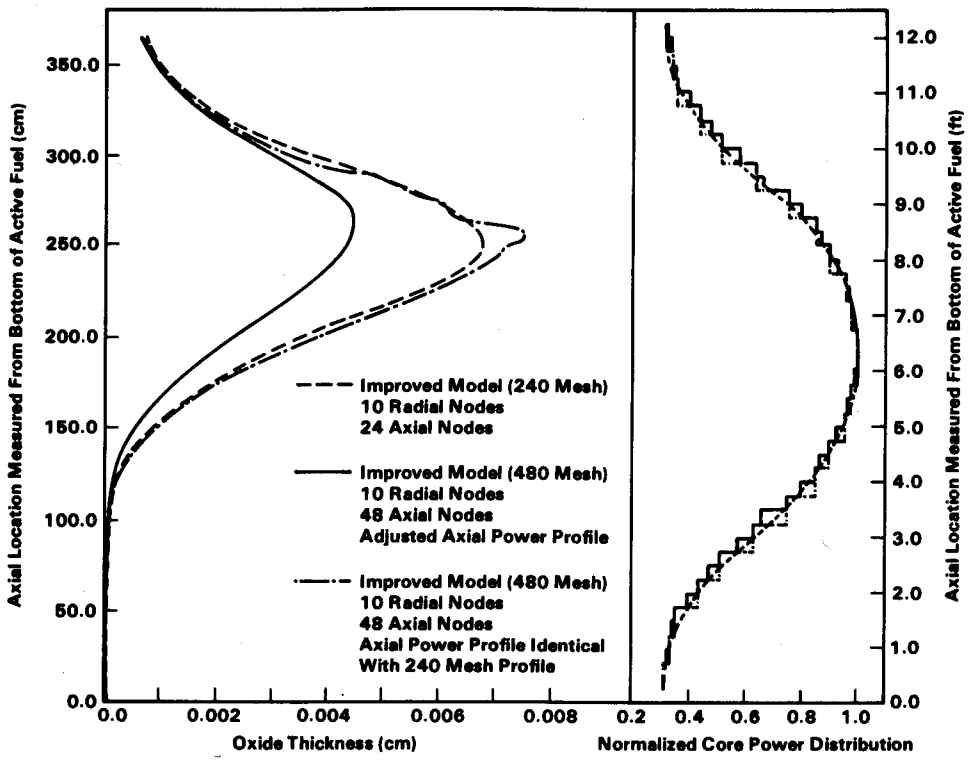

FIGURE 15. OXIDE THICKNESS AXIAL PROFILE IN THE CENTRAL RADIAL NODE FOR THE MODIFIED TML SEQUENCE AT 87 MINUTES USING THE IMPROVED MODEL. RESULTS FOR THE 48 NODE MESH ARE COMPARED WITH THE 240 NODE MESH RESULTS.